

Synergistic Bleeding Region and Point Detection in Laparoscopic Surgical Videos

Jialun Pei¹, Zhangjun Zhou², Diandian Guo¹, Zhixi Li³,
Jing Qin², Bo Du^{4†}, Pheng-Ann Heng¹

¹The Chinese University of Hong Kong ²The Hong Kong Polytechnic University

³Southern Medical University ⁴Wuhan University

dubo@whu.edu.cn

[†]Corresponding Author

Abstract

Intraoperative bleeding in laparoscopic surgery causes rapid obscuration of the operative field to hinder the surgical process and increases the risk of postoperative complications. Intelligent detection of bleeding areas can quantify the blood loss to assist decision-making, while locating bleeding points helps surgeons quickly identify the source of bleeding and achieve hemostasis in time to improve surgical success rates. In this study, we first construct a real-world laparoscopic surgical bleeding detection dataset, named **SurgBlood**, comprising 5,330 frames from 95 surgical video clips with bleeding region and point annotations. Accordingly, we develop a dual-task synergistic online detector called **BloodDet**, designed to perform simultaneous detection of bleeding regions and points in laparoscopic surgery. Our framework embraces a dual-branch bidirectional guidance design based on Segment Anything Model 2 (SAM 2). The mask branch detects bleeding regions through adaptive edge and point prompt embeddings, and the point branch leverages mask memory to induce bleeding point memory modeling and capture the direction of bleed point movement via inter-frame optical flow. By bidirectional guidance, the two branches explore potential spatial-temporal relationships while leveraging memory modeling to infer the current bleeding condition. Extensive experiments demonstrate that our baseline outperforms 12 counterparts on SurgBlood in both bleeding region and point detection. Our code and data will be publicly available.

1 Introduction

Bleeding in Laparoscopic Surgery. Minimally invasive surgery has revolutionized clinical healthcare by reducing patient trauma and accelerating postoperative recovery [36]. However, intraoperative bleeding is a common emergency that significantly impacts surgical safety and efficiency in laparoscopic surgery [13]. Rapid changes in the amount and speed of bleeding can severely obscure the surgical field, delaying the surgeon’s response and reducing the success rate of surgery. More prolonged bleeding increases the risk of organ damage and postoperative complications [11]. Therefore, utilizing computer-assisted techniques to detect bleeding regions and localize bleeding points holds significant clinical value. In one respect, detecting bleeding areas can quantify blood loss, providing timely support for intraoperative decision-making. In another respect, the precise positioning of bleeding points enables surgeons to control hemorrhage promptly to ensure surgical safety.

Challenges for Bleeding Detection. Despite the popularity of laparoscopic surgery, automated detection of bleeding regions and bleeding points still faces numerous challenges [33]. Due to the narrow field of view under laparoscopy and unstable lighting conditions, the anatomical structures are incompletely exposed, which increases the difficulty of extracting discriminative representations.

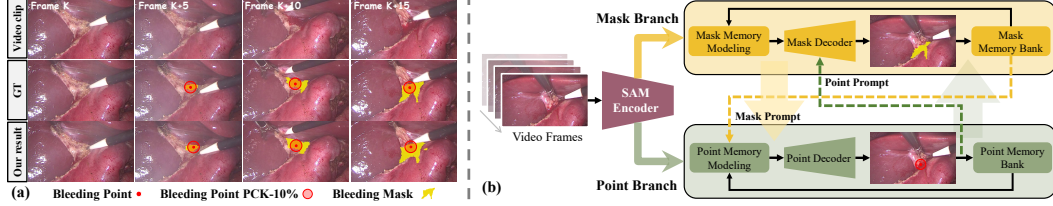


Figure 1: (a): Illustration of bleeding detection task with samples in SurgBlood and the predictions of our solution. (b): The proposed BlooDet framework performs dual-branch bidirectional guidance for the synergistic bleeding region and point detection. Zoom in for details.

Additionally, the rapid accumulation and flow of blood can change tissue appearance and infiltrate surrounding tissues, reducing the availability of low-level visual clues and complicating the detection of bleeding regions. The bleeding points may also be buried by blood or obscured by tissues, making it difficult to quickly locate and continuously track [26]. Beyond these challenges, intelligent bleeding warning involves detecting bleeding regions and locating bleeding points during dynamic surgical procedures [15]. This requires a reliable multi-task online detector that models fine-grained spatial-temporal relationships in surgical videos for accurate predictions. Further, the lack of publicly available multi-task real bleeding datasets remains a major obstacle to progress in surgical intelligence.

Proposed Benchmark. To advance research on bleeding region and point detection in surgical videos, we construct a new actual laparoscopic surgery bleeding dataset, named SurgBlood. Our dataset comprises a total of 5,330 video frames from 95 laparoscopic video clips, encompassing multiple types and intensities of bleeding during surgery. As displayed in Fig. 1(a), SurgBlood also provides pixel-level annotations of bleeding regions and bleeding point coordinates by hepatobiliary surgeons. Our dataset supports the joint detection of bleeding regions and points in video streams. We evaluate several task-relevant methods on SurgBlood to establish a comprehensive benchmark for laparoscopic intraoperative bleeding detection, driving further research in surgical assistance.

Existing Methods. Various deep learning-based algorithms have been demonstrated to be effective in bleeding region detection, including applications in intracranial hemorrhage detection [18] and bleeding detection in capsule endoscopy [3]. However, most algorithms [3, 18, 9] are designed for image or keyframe analysis, lacking the ability to model temporal dependencies in surgical videos. In addition, previous methods [30, 23, 33] mainly focus on bleeding region detection, which falls short of addressing the clinical needs in locating the bleeding source. With the emergence of large vision models, Segment Anything Model 2 (SAM 2) [29] unleashed powerful visual representation capabilities for video sequence modeling. Subsequently, a series of SAM 2-based frameworks [22, 2] have been proposed for video detection in the clinical medicine domain, but have not yet been unified into a multi-task paradigm. Some multi-task frameworks [9, 23] detect both regions and keypoints concurrently, but they overlook mutual guidance for joint optimization across tasks.

Our Solution. To meet the clinical demand of bleeding region and point detection, in this paper, we propose a dual-task online baseline model called BlooDet, which adopts a dual-branch bidirectional guidance structure based on video-level SAM 2 to synergistically optimize both tasks. As illustrated in Fig. 1(b), our framework consists of two branches: *Mask branch* and *Point branch*. In the mask branch, we embed an edge generator that performs multi-scale perception of spatial-temporal features with the Wavelet Laplacian filter to generate edge prompts, mitigating the problem of blurred bleeding boundaries in surgical scenes. Meanwhile, we incorporate bleeding points produced from the point branch as point prompts and combine them with edge prompts to facilitate bleeding region detection. For the point branch, considering the movement of bleeding points within the field of view is influenced by the relative motion of the camera, we leverage inter-frame optical flow and bleeding mask memory to estimate camera motion and viewpoint offsets, improving the location accuracy of the bleeding point and reducing interference caused by surrounding blood blurring. Further, we integrate mask memory features from the mask branch to enhance bleeding point location perception. By exchanging clues and co-guiding across two branches, BlooDet can exploits the underlying spatial and temporal associations between bleeding regions and points. Extensive experiments demonstrate that our approach achieves superior performance in both bleeding region and point detection tasks, e.g., 64.88% IoU for bleeding region detection and 83.69% PCK-10% for bleeding point detection.

The main contributions of this work are four-fold: **1)** We debut the intraoperative bleeding region and bleeding point detection tasks in surgical videos and contribute a real-world bleeding detection dataset,

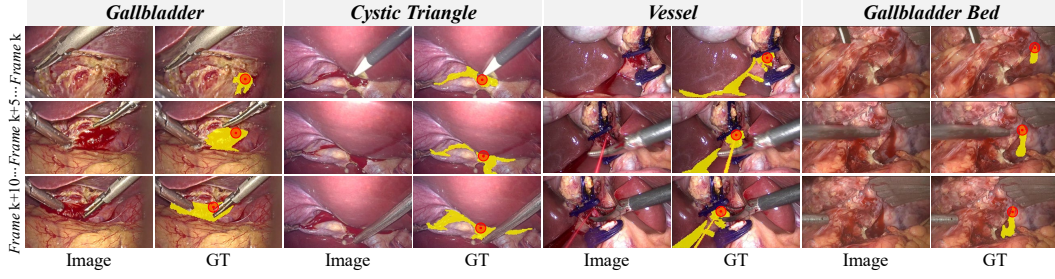


Figure 2: Illustration of bleeding types in the SurgBlood dataset. Bleeding regions and bleeding points are labeled in yellow mask and red dot.

termed SurgBlood, to advance the surgical intelligent assistance community. **2)** We propose a dual-task synergistic online detection model, BlooDet, for jointly detecting bleeding regions and points in surgical videos. Our framework embraces a dual-branch structure and performs co-optimization by mutual prompts and bidirectional guidance. **3)** The point branch utilizes inter-frame optical flow and mask memory for point memory modeling, capturing bleeding point movement cues and providing spatial-temporal modeling. Adaptive edge and point prompting strategies are introduced in the mask branch, where the edge generator exploits multi-scale Wavelet Laplacian filter to enhance edge perception, and combined with bleeding points for mask prompt embedding. **4)** We evaluate 12 task-related models and establish a comprehensive benchmark on SurgBlood. Experimental results indicate that our baseline achieves superior performance for joint bleeding region and point detection.

2 Related Work

Bleeding Region Detection in Medical Domain. Bleeding region detection has been explored across various medical scenarios, such as intracranial hemorrhage detection [18], capsule endoscopy bleeding recognition [3], and retinal hemorrhage identification [40]. Deep learning-based methods employ convolution and attention mechanisms to extract discriminative features for bleeding localization. In surgical videos, intraoperative bleeding detection presents unique challenges due to limited workspace and dynamic lighting variations. Sunakawa *et al.* [33] developed a semantic segmentation model for automatically recognizing bleeding regions on the anatomical structure of the liver. Nonetheless, existing methods primarily focus on mask-level bleeding detection, overlooking the localization of the bleeding source. To bridge this gap, we introduce a unified paradigm for the synergistic detection of bleeding regions and points in surgical videos.

Keypoint Detection in Medical Images. Keypoint detection plays a crucial role in various clinical applications, *e.g.*, pathological site identification and anatomical landmark localization [38, 1]. Existing keypoint detection methods are usually classified into three categories: 1) Context-aware spatial methods. This technique exploits the stability and uniformity of keypoint spatial distributions to improve localization accuracy [42, 21, 35, 27]. 2) Multi-stage learning strategies. These architectures follow a coarse-to-fine process to refine keypoint localization through gradual optimization and integrating shallow and deep layers to enhance performance [45, 8, 46]. 3) Multi-task learning frameworks, which jointly optimize medical image segmentation and keypoint detection by constructing a union network [43, 44, 12, 9]. Although current multi-task learning methods demonstrate strong performance, they neglect the mutual guidance between tasks. Therefore, we propose a collaborative dual-branch model that enhances both bleeding region and point detection via cross-task guidance.

Video Segmentation with Large Vision Models. With the advent of large vision models (LVMs) [16], video segmentation techniques have made great progress. Among these models, SAM 2 [29] has emerged as the leading framework, extending the capabilities of SAM from image segmentation to video domain. By leveraging large-scale pre-training and fine-tuning techniques, SAM 2 achieves state-of-the-art performance across a range of video tasks. LVM-based video segmentation techniques open up new possibilities in various downstream applications [28, 14, 7, 2, 47, 41]. SAM2-adapter [7] embeds adapter layers into SAM 2 to enhance the model’s flexibility, improving cross-task generalization. In the domain of surgical video analysis, SurgSAM-2 [22] utilizes SAM 2 along with a frame pruning mechanism for efficient instrument segmentation. Based on the powerful temporal

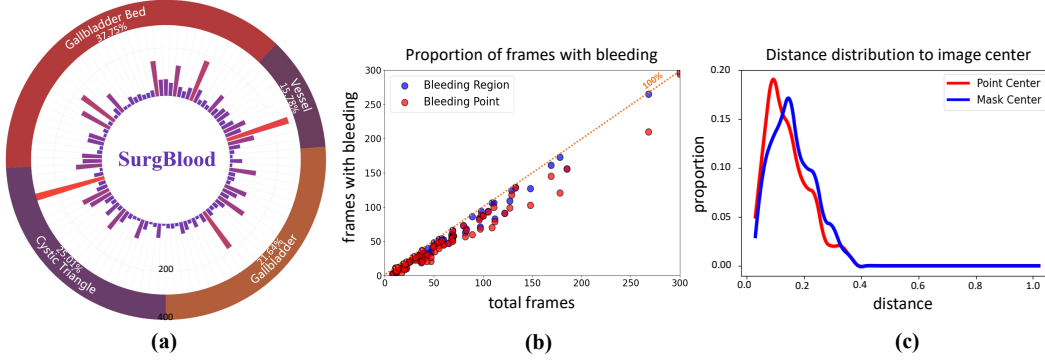


Figure 3: **Data statistics for SurgBlood.** (a) Statistical distribution of video clips; (b) Proportion of frames with bleeding region and point; (c) Distance of bleeding region and point to image center.

modeling capabilities of SAM 2, we design a dual-task paradigm that allows for joint bleeding region and point detection in complex surgical environments.

3 Proposed SurgBlood Dataset

Currently, there are few publicly available datasets for surgical bleeding detection. HemoSet [24] provides bleeding detection samples based on live animal robotic surgery, but it only includes 857 labeled frames for bleeding areas while ignoring bleeding point detection. To this end, we construct a brand-new dataset specifically for bleeding region and point detection in laparoscopic surgery, named SurgBlood. We provide an overview of our dataset from the following three aspects:

Data Collection. To ensure high-quality and representative data, we invited four hepatobiliary surgeons from partner hospitals to carefully select 95 video clips from 41 cholecystectomy surgical cases. Each clip covers the entire bleeding process while retaining the non-bleeding scene for approximately 3 seconds before and after the bleeding event. We collect a total of 5,330 video frames with a resolution of 1280×720 from all clips using a sampling rate of 2 fps. Notably, we focus exclusively on dynamic bleeding regions within the surgical action field, as this is the critical location that directly interferes with the surgeon and contains key bleeding points. As shown in Fig. 2, there are four bleeding types by tissue location: gallbladder, cystic triangle, vessel, and gallbladder bed. The proportion of bleeding types corresponds to the frequency distribution observed in actual surgery.

Data Annotation. To ensure the annotation quality of SurgBlood, the invited hepatobiliary surgeons meticulously annotate and review each video clip. During the labeling process, the surgeon uses both static frames and dynamic video sequences to label bleeding regions and bleeding point coordinates for each frame. Annotation is guided by the following principles: 1) For bleeding regions, pooled blood and inactive sparse bloodstains are not annotated. 2) For bleeding points, if the bleeding point is not obscured by tissue or instruments, its coordinates are labeled; if the bleeding point is obscured by blood, annotators trace back to the first frame where the bleeding occurred and localize the point based on the surrounding anatomy. These situations bring distinct characteristics and challenges to our dataset. To ensure annotation consistency, we adopt the cross-validation strategy: each clip is initially annotated by four surgeons, followed by a review and refinement process conducted by two additional surgeons. Fig. 2 presents examples of annotations for various bleeding situations. All data has been approved by the ethics statement and will be available.

Data Analysis. 1) *Clip Distribution:* SurgBlood includes 5,330 frames extracted from 95 video clips. As shown in Fig. 3(a), each clip contains an average of 56 frames, with the longest containing 300 frames and the shortest containing 8 frames. We also counted the distribution of bleeding types: gallbladder (21.64%), cystic triangle (25.01%), vessel (15.78%), and gallbladder bed (37.75%).

2) *Bleeding Ratio:* We calculate the proportion of frames containing bleeding regions and points. As shown on the left of Fig. 3(b), both bleeding regions and points have a high frame rate, where the slightly higher rate with bleeding regions is due to the partial occlusion of bleeding points.

3) *Space Statistics:* We analyze the spatial distribution and center bias of bleeding regions and points across all samples in SurgBlood. The right of Fig. 3(c) provides statistical insights into the distances

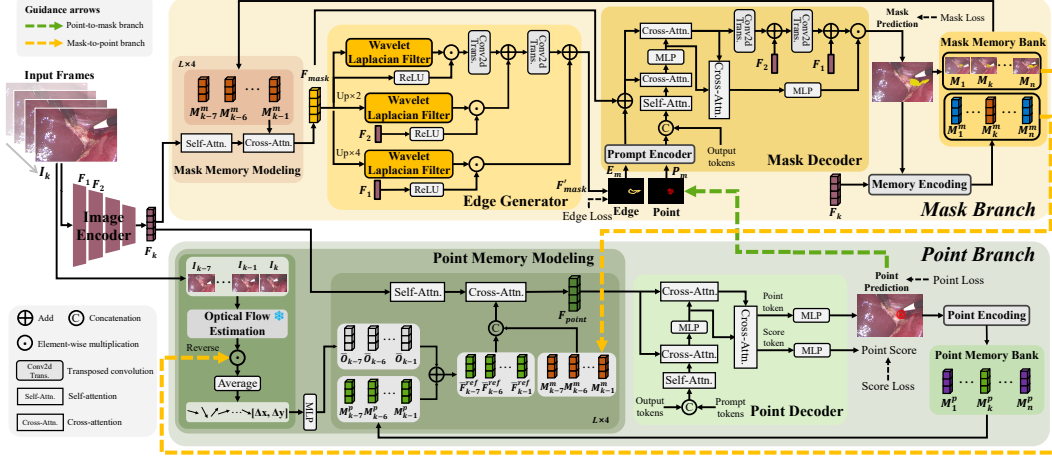


Figure 4: Overview of the proposed BlooDet. Our framework comprises a mask branch and a point branch to jointly detect bleeding regions and bleeding points. Cross-branch guidance and adaptive prompt embedding allow our framework to reach a co-optimized state. Zoom in for details.

of bleeding region centers and bleeding points from the image center. We can see that bleeding caused by surgical operations predominantly occurs near the image center, and bleeding points are contained within bleeding regions for the vast majority of the time.

4 Proposed Method

4.1 Overall Architecture

BlooDet is a dual-task collaborative detector for simultaneous bleeding region and point detection in surgical videos. As shown in Fig. 4, our framework revises the body of SAM 2 [29] by empowering edge clues to detect bleeding regions and incorporating a point branch to detect bleeding points. The whole model consists of the following processes: image encoder, mask/point memory modeling, Edge generator, mask/point decoder, and mask/point memory bank.

Image Encoding. Given a set of N video frames, including the current frame $I_k \in \mathbb{R}^{H \times W \times 3}$ and the previous $N-1$ frames $X = \{I_i\}_{i=k-N+1}^{k-1}$, we first flatten frames and feed them into the image encoder inherited from SAM 2 to produce multi-scale spatial features $F \in \mathbb{R}^{s \times c \times N}$, where s denotes the length of the feature sequence and c is the feature dimension. Then, the output sequential frame features F_{k-N}, \dots, F_k are fed into the mask and point branches, respectively, for memory modeling.

Point Branch. As shown in the bottom of Fig. 4, the point branch comprises three main parts: point memory modeling, point decoder, and point memory bank. Compared to mask memory modeling, the point memory modeling module embeds optical flow estimation to predict the displacement field between consecutive frames $[I_{k-7}, \dots, I_k]$, enabling the inference of laparoscopic camera motion and viewpoint offset during surgery, thereby identifying the movement direction of current bleeding points. Further, we integrate previous mask memory features $\{M_q^m\}_{q=k-7}^{k-1}$ from mask branch with the corresponding point features to enhance location and temporal perception as well as to narrow the search space for bleeding point coordinates. We describe this process in detail in Sec. 4.2.

Afterward, the memory-enhanced point feature F_{point} passes through the point decoder to predict the bleeding point. Different from the upsampling fusion in the mask decoder, we employ learnable output tokens and prompt tokens consistent with SAM 2 that interact with F_{point} through self-attention and cross-attention operations [5], followed by MLP layers to predict bleeding point coordinates and confidence scores. The point memory is stored in the point memory bank for temporal modeling.

Mask Branch. This branch focuses on predicting bleeding regions by mask memory modeling and coupling bleeding edge and point prompts. The top of Fig. 4 illustrates the pipeline of our mask branch. The current frame features F_k are first fed into mask memory modeling to perform self- and cross-attention interaction [37] with mask memory features from previous frames, producing the spatial-temporal feature F_{mask} . After that, we introduce an edge generator that adopts multi-scale

Wavelet Laplacian filters to F_{mask} for edge refinement. Then, we incorporate high-resolution features from the image encoder to obtain edge maps (detailed description in Sec. 4.3). Unlike the manual intervention prompts in SAM [16, 29], we form adaptive prompt embeddings by combining the edge map E_m from the edge generator with the point map P_m output from point branch. Then, the prompt encoder is utilized to encode E_m and P_m to yield prompt features E_p and P_p :

$$E_p, P_p = \mathcal{P}[E_m, P_m], \quad (1)$$

$$E_p = \text{Conv}(\text{LN}(\mathbf{G}(\text{Conv}(\text{LN}(\mathbf{G}(\text{Conv}(E_m))))))), \quad (2)$$

$$P_p = \mathcal{C}[\sin(2\pi(\text{Po}(P_m))), \cos(2\pi(\text{Po}(P_m)))] + \text{Le}, \quad (3)$$

where \mathcal{P} represents prompt encoding, \mathbf{G} denotes the GeLU function, Conv refers to 2×2 convolution operation, and LN is layer normalization. Also, Po denotes positional encoding [34], Le stands for learned embeddings, and $\mathcal{C}[\cdot]$ is the concatenation operation. We input prompt features along with F_{mask} into the mask decoder and attain the predicted bleeding mask by upsampling and integrating with high-resolution features. Subsequently, we employ memory encoding to achieve the mask memory feature M_k^m and store it in the mask memory bank. Further, the mask maps are also updated in the mask memory bank to provide spatial guidance for bleeding point detection.

Cross-branch Guidance. Our framework embraces bidirectional collaborative guidance between masks and point branches, enabling simultaneous optimization of bleeding region and bleeding point predictions. For the mask decoder, we exploit the point map produced by the point decoder as an automatic prompt input. This helps guide the decoder to focus on the target bleeding region while mitigating the interference from residual blood in the surrounding area. In point memory modeling, the predicted mask maps from previous frames can assist in optical flow estimation and in predicting the direction of the bleeding point. Besides, mask memory features are merged with point memory features to induce the point decoder to concentrate on the most likely bleeding areas while mitigating the impact of low-contrast background. With cross-branch guidance, both branches are synergistically optimized, yielding consistent bleeding region and point predictions across consecutive frames.

4.2 Point Memory Modeling in Point Branch

To detect bleeding points in consecutive frames effectively, we embed the point memory modeling module in the point branch to develop temporal clues for point features. As illustrated in Fig. 4, point memory modeling is divided into two steps: 1) combining the optical flow between consecutive frames with region maps to compensate for the relative displacement of the bleeding point caused by camera viewpoint offset, 2) interacting the average camera displacement of previous frames with mask memory features from mask branch to obtain point memory features.

For the viewpoint offset of the camera, we first utilize the frozen PWC-Net [31] for optical flow estimation. Given N frames $\{I_i\}_{i=k-N+1}^k$, the optical flow $O_i(x, y) \in \mathbb{R}^{H \times W \times 2}$ between two consecutive frames can be expressed as $O_i(x, y) = \text{PWC-Net}(I_{i-1}, I_i)$. Considering the instability of the optical flow in the rapidly changing bleeding region, we reverse the mask map M_i from mask branch for each frame and combine with $O_i(x, y)$ to obtain the average viewpoint offset $\bar{O}_i(\Delta x, \Delta y)$:

$$\bar{O}_i(\Delta x, \Delta y) = \frac{1}{H \times W} \sum_{X=1}^H \sum_{Y=1}^W (1 - M_i) \cdot O_i(x, y). \quad (4)$$

Then, the global offset coordinates $\bar{O}_i \in \mathbb{R}^2$ of previous frames can be produced via an MLP layer.

After that, we aggregate point memory features M_i^p of previous frames in the point memory bank with \bar{O}_i and concatenate with mask memory features M_i^m to obtain the mask-guided corrected point features \bar{F}_i^{ref} . Lastly, we perform a self-attention operation on F_k and cross-attention with \bar{F}_i^{ref} to the memory-enhanced point feature F_{point} . Through the motion compensation mechanism based on optical flow estimation together with cross-branch mask guidance, we perform effective memory modeling of bleeding point features in laparoscopic scenes with camera offset.

4.3 Edge Generator in Mask Branch

Detecting bleeding regions is challenging due to the low contrast and high noise in surgical scenes. To this end, we embed a dedicated edge generator in the mask branch, which enhances the accuracy

of bleeding region detection by combining multi-scale Wavelet Laplacian filters [17] with high-resolution features containing lower-level texture clues to generate edge map prompts. Concretely, we first input the spatial-temporal features F_{mask} into the Gabor Wavelet Laplacian filter to enhance edge structures in the spatial domain. The Gabor Wavelet operation on the spatial position (x, y) is calculated as

$$\mathcal{G}(x, y; \lambda, \theta, \psi, \sigma, \gamma) = \exp\left(-\frac{x'^2 + \gamma^2 y'^2}{2\sigma^2}\right) \exp\left(i\left(\frac{2\pi}{\lambda}x' + \psi\right)\right), \quad (5)$$

where $x' = x\cos\theta + y\sin\theta$, $y' = -x\sin\theta + y\cos\theta$, λ denotes the wavelength, θ is the orientation angle of the Gabor kernel, ψ is the phase offset, σ is the standard deviation of Gaussian function, and γ stands for the aspect ratio. Therefore, Laplacian filtering based on the Gabor wavelet is defined as

$$\mathbf{L}_g(x, y) = \Delta f(x, y) \cdot \mathcal{G}(x, y), \quad (6)$$

$$\Delta f(x, y) = \frac{\partial^2 f}{x^2} + \frac{\partial^2 f}{y^2}, \quad (7)$$

where $\Delta f(x, y)$ represents the Laplacian operator in 2D space. Then, we perform an activation operation on F_{mask} and interact with the filtered features to suppress low-confidence signals and preserve refined edge features. The whole process of the edge generator can be described as

$$F'_{mask} = (\text{ReLU}(F_{mask})) \odot (\mathbf{L}_g(x, y) * F_{mask}), \quad (8)$$

where \odot and $*$ denote the element-wise multiplication and convolution operation. The feature F'_{mask} represents the output from the edge generator. As illustrated in Fig. 4, we parallel upsample F'_{mask} twice and separately pass through the Wavelet Laplace filters, and then interact with high-resolution features, *i.e.*, F_1 and F_2 , to further refine the edge information. Finally, the generated edge map is fed into the mask decoder as the edge prompt for bleeding region detection.

4.4 Loss Function

The total loss function of BlooDet consists of mask loss \mathcal{L}_{mask} and edge loss \mathcal{L}_{edge} from mask branch, as well as point loss \mathcal{L}_{point} and score loss \mathcal{L}_{score} from point branch:

$$\mathcal{L} = \lambda_m \mathcal{L}_{mask} + \lambda_e \mathcal{L}_{edge} + \lambda_s \mathcal{L}_{score} + \lambda_p \mathcal{L}_{point}. \quad (9)$$

Both \mathcal{L}_{mask} and \mathcal{L}_{edge} are computed as a combination of Focal loss [20] and Dice loss [25]. In addition, \mathcal{L}_{point} employs the smooth L1 loss for point-level supervision:

$$\mathcal{L}_{point} = \sum_{i=1}^N \mathbf{1}_{\{p_i \neq [0,0]\}} \cdot L1(\hat{y}_p^i, y_p^i), \quad (10)$$

where \hat{y}_p^i is the predicted point location and y_p^i is the ground-truth point location. $\mathbf{1}_{\{p_i \neq [0,0]\}}$ denotes an indicator function that ensures the loss is calculated only when the point is not zero. Besides, \mathcal{L}_{score} is the binary cross-entropy loss for point existence in point branch. λ_m , λ_e , λ_s , and λ_p are empirically set to 1, 1, 1, and 0.5, respectively, to balance the total loss function.

5 Experiments

5.1 Datasets and Evaluation Metrics

Datasets. Since the tasks of the laparoscopic bleeding region and bleeding point cooperative detection are proposed for the first time, we adopt the proposed SurgBlood dataset to train and test our method and related comparative methods. We randomly split a total of 95 video clips into two sets: 75 for training and the remaining 20 for testing.

Evaluation Metrics. Following previous studies [29, 9], we adopt the Intersection over Union (IoU) and Dice Coefficient (Dice) metrics to evaluate bleeding region detection performance. For bleeding points, the Percentage of Correct Keypoints (PCK) metric is used to measure localization accuracy. Unlike the 10% to 40% threshold range applied in [9, 23] for anatomical structure centroids, we adopt a narrower threshold range of 2%–10% to ensure greater assessment, *i.e.*, PCK-2%, PCK-5%, and PCK-10%. This is due to the requirement for higher precision and lower tolerance of bleeding point detection in laparoscopic surgery.

Table 1: Overall comparison with well-known task-related methods on SurgBlood test set. SAM 2[†] denotes SAM 2_base with an additional point head.

Types	Methods	Volumes	Bleeding Region Metrics		Bleeding Point Metrics			Params (M) ↓
			IoU ↑	Dice ↑	PCK-2% ↑	PCK-5% ↑	PCK-10% ↑	
Region-level	Swin-UNet [4]	ECCV'22	41.31	58.47	-	-	-	27.2
	SAM [16]	ICCV'23	40.43	57.49	-	-	-	93.7
	SAM-Adapter [6]	ICCV'23	54.80	70.80	-	-	-	93.8
	MemSAM [10]	CVPR'24	55.34	71.28	-	-	-	133.3
	SAM 2 [29]	ICLR'25	63.51	77.68	-	-	-	80.8
	SAM2-Adapter [7]	arXiv'24	64.23	77.95	-	-	-	88.8
Point-level	HRNet [32]	CVPR'19	-	-	3.13	15.98	44.31	63.6
	SimCC [19]	ECCV'22	-	-	2.14	14.99	46.95	66.3
	GTPT [39]	ECCV'24	-	-	2.80	13.01	38.38	16.7
	D-CeLR [8]	ECCV'24	-	-	5.10	27.67	60.13	53.4
Multi-task	PAINet [9]	MICCAI'23	44.14	61.24	2.47	15.48	48.43	13.6
	PitSurgRT [23]	IJCARS'24	30.48	46.72	2.47	13.84	41.68	67.3
	SAM 2 [†] [29]	ICLR'25	50.93	67.49	12.35	41.68	71.99	81.0
	BlooDet (Ours)	-	64.88	78.70	18.62	55.85	83.69	91.6

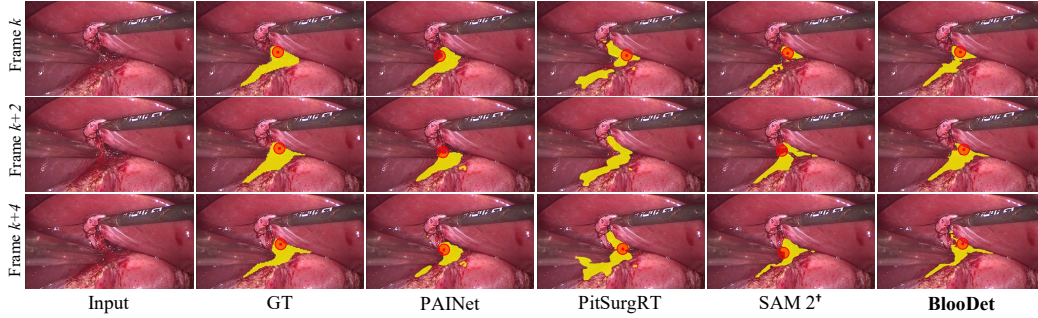


Figure 5: Visual comparison of bleeding region and point detection on SurgBlood test set.

5.2 Implementation Details

Our framework is implemented on a single RTX 4090 GPU. During training, we input eight consecutive frames in an online manner with resolution resized to 512×512 pixels. The image encoder of BlooDet is initialized with pre-trained weights from SAM 2_base [29]. Additionally, we utilize a frozen PWC-Net [31] to compute inter-frame optical flow. No data augmentation is applied during data loading. The maximum learning rate for the image encoder is set to $5e-6$, while other parts are trained with $5e-4$. We employ the Adam optimizer with a warm-up strategy and linear decay, training for 20 epochs. During inference, we perform frame-by-frame inference in line with SAM 2.

5.3 Performance on SurgBlood Benchmark

We evaluate 12 task-related methods for bleeding region and point detection to build a comprehensive benchmark on SurgBlood, including multi-task detection models [9, 23], video- and image-level object segmentation methods [4, 16, 29, 6, 10, 7], and pose-based point detection methods [32, 19, 39, 8]. For fairness, all methods use the official code and adapt only the head to fit bleeding tasks.

Quantitative Evaluation. Table 1 presents the performance of our framework and other comparison methods on SurgBlood test set for bleeding region and point detection. Our framework outperforms competitors across both tasks, even surpassing models designed for a single task. Benefiting from edge-enhanced prompts and bleeding point guidance, BlooDet achieves notable improvements in bleeding region detection. For bleeding point detection, BlooDet significantly surpasses other methods, with 6.27% and 14.17% improvement in PCK-2% and PCK-5% metrics, respectively. Besides, our framework obtains superior performance while adding a few parameters.

Qualitative Evaluation. Fig. 5 shows a visual comparison of our approach with other multi-task frameworks. We can see that BlooDet provides greater stability and consistency in detecting bleeding regions and points. In complex surgical environments with low contrast, competitors tend to be disturbed by surrounding noise. In contrast, our method ensures robust detection across consecutive frames via spatial-temporal modeling and co-guidance.

EG	PMM	IoU \uparrow	Dice \uparrow	PCK-2% \uparrow	PCK-5% \uparrow	PCK-10% \uparrow
\times	\times	50.93	67.49	12.35	41.68	71.99
\checkmark	\times	64.78	78.36	8.23	40.04	75.94
\times	\checkmark	61.20	75.93	14.33	51.57	80.89
\checkmark	\checkmark	64.88	78.70	18.62	55.85	83.69

Table 2: Ablations for key components of BlooDet. EG and PMM denote edge generator and point memory modeling modules.

Configs	IoU \uparrow	Dice \uparrow	# Params (M)
w/o Edge generator	61.20	75.93	90.99
w/o Laplacian Filter	60.79	75.61	91.58
w/o F_1 & F_2	64.74	78.60	91.55
Edge generator	64.88	78.70	91.58

Table 3: Influence of edge generator for bleeding region detection.

Mask map	PCK-2% \uparrow	PCK-5% \uparrow	PCK-10% \uparrow
Foreground	12.03	41.02	71.99
Background	18.62	55.85	83.69
Global	15.49	49.59	82.00

Table 4: Ablations for optical flow operation.

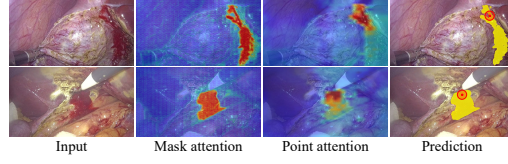


Figure 6: Attention maps in mask and point branches of BlooDet.

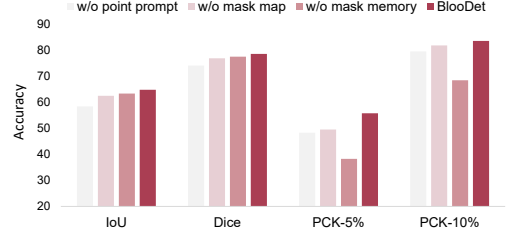


Figure 7: Effect of mutual guidance between mask and point branches of BlooDet.

5.4 Ablation Analysis

Contributions of Key Component. Table 2 illustrates the contribution of key components in BlooDet. The experimental results show that point memory modeling contributes significantly to detecting bleeding points, *e.g.*, improving the PCK-2% score by about 10.4%. Moreover, our edge generator provides effective edge prompt embedding, which greatly improves the accuracy of bleeding region detection. In short, each key component contributes positively to model performance.

Ablations for Edge Generator. We investigate the effect of different edge generator designs embedded in the mask branch. As exhibited in Table 3, the Wavelet Laplacian filter shows a strong response to edge clues, effectively mitigating interference from complex backgrounds in laparoscopic scenes. Meanwhile, integrating high-resolution features further enhances the quality of edge maps.

Optical Flow Operation Design. In point memory modeling, we adopt reversed mask maps in conjunction with optical flow maps to estimate the average camera displacement. To validate the effect of this design, we ablate the impact of focusing on different regions in mask maps for bleeding point detection. Table 4 indicates that using the foreground region leads to inferior performance. It may be explained by the poor stability of optical flow in the rapidly changing bleeding area. In contrast, utilizing the background enables more stable motion modeling and point localization.

Effect of Bidirectional Guidance. To validate the effectiveness of our cross-branch bidirectional guidance, Fig. 7 ablates the impact of point prompt from point branch as well as mask map and mask memory from mask branch. The results indicate that the point prompt contributes to bleeding region detection. For the point branch, the mask maps from previous frames assist with the optical flow operation, while mask memory fosters point memory modeling to improve the accuracy of point localization. It also illustrates that the proposed dual-branch collaborative structure is superior to a single-branch design. The attention maps from the mask and point decoders visualized in Fig. 6 also verify the effect of bidirectional guidance.

6 Conclusion

This work advances the intelligent detection of bleeding regions and bleeding points in laparoscopic surgical videos. We first contribute an open-source dataset for bleeding detection in real surgical scenarios, SurgBlood, to facilitate benchmark construction. Accordingly, we design a dual-task synergistic online framework called BlooDet, which assembles mask and point branches in a bidirectional guidance structure, and exploits an edge generator and point memory modeling to enhance the adaptive prompting scheme. Extensive experimental results demonstrate that our method outperforms existing models for both bleeding tasks. We believe this study can facilitate research in intelligent surgical assistance, reducing intraoperative decision-making risks and improving clinical outcomes.

References

- [1] Sharib Ali, Yamid Espinel, Yueming Jin, Peng Liu, Bianca Güttner, Xukun Zhang, Lihua Zhang, Tom Dowrick, Matthew J Clarkson, Shiting Xiao, et al. An objective comparison of methods for augmented reality in laparoscopic liver resection by preoperative-to-intraoperative image fusion from the miccai2022 challenge. *Medical Image Analysis*, 99:103371, 2025.
- [2] Yunhao Bai, Qinji Yu, Boxiang Yun, Dakai Jin, Yingda Xia, and Yan Wang. Fs-medsam2: Exploring the potential of sam2 for few-shot medical image segmentation without fine-tuning. *arXiv preprint arXiv:2409.04298*, 2024.
- [3] N Bourbakis, Sokratis Makrogiannis, and Despina Kavraki. A neural network-based detection of bleeding in sequences of wce images. In *Fifth IEEE Symposium on Bioinformatics and Bioengineering*, pages 324–327, 2005.
- [4] Hu Cao, Yueyue Wang, Joy Chen, Dongsheng Jiang, Xiaopeng Zhang, Qi Tian, and Manning Wang. Swin-unet: Unet-like pure transformer for medical image segmentation. In *ECCV*, 2022.
- [5] Nicolas Carion, Francisco Massa, Gabriel Synnaeve, Nicolas Usunier, Alexander Kirillov, and Sergey Zagoruyko. End-to-end object detection with transformers. In *ECCV*, pages 213–229, 2020.
- [6] Tianrun Chen, Lanyun Zhu, Chaotao Deng, Runlong Cao, Yan Wang, Shangzhan Zhang, Zejian Li, Lingyun Sun, Ying Zang, and Papa Mao. Sam-adapter: Adapting segment anything in underperformed scenes. In *IEEE ICCV*, pages 3367–3375, 2023.
- [7] Tianrun Chen, Ankang Lu, Lanyun Zhu, Chaotao Ding, Chunan Yu, Deyi Ji, Zejian Li, Lingyun Sun, Papa Mao, and Ying Zang. Sam2-adapter: Evaluating & adapting segment anything 2 in downstream tasks: Camouflage, shadow, medical image segmentation, and more. *arXiv preprint arXiv:2408.04579*, 2024.
- [8] Chao Dai, Yang Wang, Chaolin Huang, Jiakai Zhou, Qilin Xu, and Minpeng Xu. A cephalometric landmark regression method based on dual-encoder for high-resolution x-ray image. In *ECCV*, pages 93–109, 2024.
- [9] Adrito Das, Danyal Z Khan, Simon C Williams, John G Hanrahan, Anouk Borg, Neil L Dorward, Sophia Bano, Hani J Marcus, and Danail Stoyanov. A multi-task network for anatomy identification in endoscopic pituitary surgery. In *MICCAI*, pages 472–482, 2023.
- [10] Xiaolong Deng, Huisi Wu, Runhao Zeng, and Jing Qin. Memsam: taming segment anything model for echocardiography video segmentation. In *IEEE CVPR*, pages 9622–9631, 2024.
- [11] Daniel J Deziel, Keith W Millikan, Steven G Economou, Alexander Doolas, Sung-Tao Ko, and Mohan C Airan. Complications of laparoscopic cholecystectomy: a national survey of 4,292 hospitals and an analysis of 77,604 cases. *The American Journal of Surgery*, 165(1):9–14, 1993.
- [12] Jinming Duan, Ghalib Bello, Jo Schlemper, Wenjia Bai, Timothy JW Dawes, Carlo Biffi, Antonio de Marvao, Georgia Doumoud, Declan P O’Regan, and Daniel Rueckert. Automatic 3d bi-ventricular segmentation of cardiac images by a shape-refined multi-task deep learning approach. *IEEE TMI*, 38(9):2151–2164, 2019.
- [13] Jared R Gallaher and Anthony Charles. Acute cholecystitis: a review. *Jama*, 327(10):965–975, 2022.
- [14] Ziyu Guo, Renrui Zhang, Xiangyang Zhu, Chengzhuo Tong, Peng Gao, Chunyuan Li, and Pheng-Ann Heng. Sam2point: Segment any 3d as videos in zero-shot and promptable manners. *arXiv preprint arXiv:2408.16768*, 2024.
- [15] Yuichiro Hirai, Ai Fujimoto, Naomi Matsutani, Soichiro Murakami, Yuki Nakajima, Ryoichi Miyanaga, Yoshihiro Nakazato, Kazuyo Watanabe, Masahiro Kikuchi, and Naohisa Yahagi. Evaluation of the visibility of bleeding points using red dichromatic imaging in endoscopic hemostasis for acute gi bleeding (with video). *Gastrointestinal Endoscopy*, 95(4):692–700, 2022.

- [16] Alexander Kirillov, Eric Mintun, Nikhila Ravi, Hanzi Mao, Chloe Rolland, Laura Gustafson, Tete Xiao, Spencer Whitehead, Alexander C Berg, Wan-Yen Lo, et al. Segment anything. In *IEEE ICCV*, pages 4015–4026, 2023.
- [17] Tai Sing Lee. Image representation using 2d gabor wavelets. *IEEE TPAMI*, 18(10):959–971, 1996.
- [18] Lu Li, Meng Wei, BO Liu, Kunakorn Atchaneeyasakul, Fugen Zhou, Zehao Pan, Shimran A Kumar, Jason Y Zhang, Yuehua Pu, David S Liebeskind, et al. Deep learning for hemorrhagic lesion detection and segmentation on brain ct images. *IEEE JBHI*, 25(5):1646–1659, 2020.
- [19] Yanjie Li, Sen Yang, Peidong Liu, Shoukui Zhang, Yunxiao Wang, Zhicheng Wang, Wankou Yang, and Shu-Tao Xia. Simcc: A simple coordinate classification perspective for human pose estimation. In *ECCV*, pages 89–106, 2022.
- [20] Tsung-Yi Lin, Priya Goyal, Ross Girshick, Kaiming He, and Piotr Dollár. Focal loss for dense object detection. In *IEEE ICCV*, pages 2980–2988, 2017.
- [21] Chuanbin Liu, Hongtao Xie, Sicheng Zhang, Jingyuan Xu, Jun Sun, and Yongdong Zhang. Misshapen pelvis landmark detection by spatial local correlation mining for diagnosing developmental dysplasia of the hip. In *MICCAI*, pages 441–449, 2019.
- [22] Haofeng Liu, Erli Zhang, Junde Wu, Mingxuan Hong, and Yueming Jin. Surgical sam 2: Real-time segment anything in surgical video by efficient frame pruning. In *NeurIPS Workshop*, 2024.
- [23] Zhehua Mao, Adrito Das, Mobarakol Islam, Danyal Z Khan, Simon C Williams, John G Hanrahan, Anouk Borg, Neil L Dorward, Matthew J Clarkson, Danail Stoyanov, et al. Pitsurgtr: real-time localization of critical anatomical structures in endoscopic pituitary surgery. *IJCARS*, pages 1–8, 2024.
- [24] Albert J Miao, Shan Lin, Jingpei Lu, Florian Richter, Benjamin Ostrander, Emily K Funk, Ryan K Orosco, and Michael C Yip. Hemoset: The first blood segmentation dataset for automation of hemostasis management. In *ISMR*, pages 1–7, 2024.
- [25] Fausto Milletari, Nassir Navab, and Seyed-Ahmad Ahmadi. V-net: Fully convolutional neural networks for volumetric medical image segmentation. In *3DV*, pages 565–571, 2016.
- [26] Yosuke Mori, Taro Iwatsubo, Akitoshi Hakoda, Shin Kameishi, Kazuki Takayama, Shun Sasaki, Ryoji Koshiba, Shinya Nishida, Satoshi Harada, Hironori Tanaka, et al. Red dichromatic imaging improves the recognition of bleeding points during endoscopic submucosal dissection. *Digestive Diseases and Sciences*, 69(1):216–227, 2024.
- [27] Jialun Pei, Ruize Cui, Yaoqian Li, Weixin Si, Jing Qin, and Pheng-Ann Heng. Depth-driven geometric prompt learning for laparoscopic liver landmark detection. In *MICCAI*, pages 154–164, 2024.
- [28] Jialun Pei, Zhangjun Zhou, and Tiantian Zhang. Evaluation study on sam 2 for class-agnostic instance-level segmentation. *arXiv preprint arXiv:2409.02567*, 2024.
- [29] Nikhila Ravi, Valentin Gabeur, Yuan-Ting Hu, Ronghang Hu, Chaitanya Ryali, Tengyu Ma, Haitham Khedr, Roman Rädle, Chloe Rolland, Laura Gustafson, et al. Sam 2: Segment anything in images and videos. In *ICLR*, 2025.
- [30] Ruisheng Su, Matthijs van der Sluijs, Sandra AP Cornelissen, Geert Lycklama, Jeannette Hofmeijer, Charles BLM Majoie, Pieter Jan van Doormaal, Adriaan CGM Van Es, Danny Ruijters, Wiro J Niessen, et al. Spatio-temporal deep learning for automatic detection of intracranial vessel perforation in digital subtraction angiography during endovascular thrombectomy. *Medical Image Analysis*, 77:102377, 2022.
- [31] Deqing Sun, Xiaodong Yang, Ming-Yu Liu, and Jan Kautz. Pwc-net: Cnns for optical flow using pyramid, warping, and cost volume. In *IEEE CVPR*, pages 8934–8943, 2018.

- [32] Ke Sun, Bin Xiao, Dong Liu, and Jingdong Wang. Deep high-resolution representation learning for human pose estimation. In *IEEE CVPR*, pages 5693–5703, 2019.
- [33] Taiki Sunakawa, Daichi Kitaguchi, Shin Kobayashi, Keishiro Aoki, Manabu Kujiraoka, Kimimasa Sasaki, Lena Azuma, Atsushi Yamada, Masashi Kudo, Motokazu Sugimoto, et al. Deep learning-based automatic bleeding recognition during liver resection in laparoscopic hepatectomy. *Surgical Endoscopy*, pages 1–7, 2024.
- [34] Matthew Tancik, Pratul Srinivasan, Ben Mildenhall, Sara Fridovich-Keil, Nithin Raghavan, Utkarsh Singhal, Ravi Ramamoorthi, Jonathan Barron, and Ren Ng. Fourier features let networks learn high frequency functions in low dimensional domains. *NeurIPS*, 33:7537–7547, 2020.
- [35] Ahmet Tuysuzoglu, Jeremy Tan, Kareem Eissa, Atilla P Kiraly, Mamadou Diallo, and Ali Kamen. Deep adversarial context-aware landmark detection for ultrasound imaging. In *MICCAI*, pages 151–158, 2018.
- [36] Chris Varghese, Ewen M Harrison, Greg O’Grady, and Eric J Topol. Artificial intelligence in surgery. *Nature Medicine*, pages 1–12, 2024.
- [37] Ashish Vaswani, Noam Shazeer, Niki Parmar, Jakob Uszkoreit, Llion Jones, Aidan N Gomez, Łukasz Kaiser, and Illia Polosukhin. Attention is all you need. *NeurIPS*, 30, 2017.
- [38] Eugene Vorontsov, Aican Bozkurt, Adam Casson, George Shaikovski, Michal Zelechowski, Kristen Severson, Eric Zimmermann, James Hall, Neil Tenenholtz, Nicolo Fusi, et al. A foundation model for clinical-grade computational pathology and rare cancers detection. *Nature Medicine*, 30(10):2924–2935, 2024.
- [39] Haonan Wang, Jie Liu, Jie Tang, Gangshan Wu, Bo Xu, Yanbing Chou, and Yong Wang. Gtpt: Group-based token pruning transformer for efficient human pose estimation. In *ECCV*, pages 213–230, 2024.
- [40] Renkai Wu, Pengchen Liang, Yiqi Huang, Qing Chang, and Huiping Yao. Automatic segmentation of hemorrhages in the ultra-wide field retina: multi-scale attention subtraction networks and an ultra-wide field retinal hemorrhage dataset. *IEEE JBHI*, 2024.
- [41] Xinyu Xiong, Zihuang Wu, Shuangyi Tan, Wenxue Li, Feilong Tang, Ying Chen, Siying Li, Jie Ma, and Guanbin Li. Sam2-unet: Segment anything 2 makes strong encoder for natural and medical image segmentation. *arXiv preprint arXiv:2408.08870*, 2024.
- [42] Dongqing Zhang, Jianing Wang, Jack H Noble, and Benoit M Dawant. Headlocnet: Deep convolutional neural networks for accurate classification and multi-landmark localization of head cts. *Medical Image Analysis*, 61:101659, 2020.
- [43] Jun Zhang, Mingxia Liu, Li Wang, Si Chen, Peng Yuan, Jianfu Li, Steve Guo-Fang Shen, Zhen Tang, Ken-Chung Chen, James J Xia, et al. Joint craniomaxillofacial bone segmentation and landmark digitization by context-guided fully convolutional networks. In *MICCAI*, pages 720–728, 2017.
- [44] Jun Zhang, Mingxia Liu, Li Wang, Si Chen, Peng Yuan, Jianfu Li, Steve Guo-Fang Shen, Zhen Tang, Ken-Chung Chen, James J Xia, et al. Context-guided fully convolutional networks for joint craniomaxillofacial bone segmentation and landmark digitization. *Medical Image Analysis*, 60:101621, 2020.
- [45] Yefeng Zheng, David Liu, Bogdan Georgescu, Hien Nguyen, and Dorin Comaniciu. 3d deep learning for efficient and robust landmark detection in volumetric data. In *MICCAI*, pages 565–572, 2015.
- [46] Zhushi Zhong, Jie Li, Zhenxi Zhang, Zhicheng Jiao, and Xinbo Gao. An attention-guided deep regression model for landmark detection in cephalograms. In *MICCAI*, pages 540–548, 2019.
- [47] Jiayuan Zhu, Yunli Qi, and Junde Wu. Medical sam 2: Segment medical images as video via segment anything model 2. *arXiv preprint arXiv:2408.00874*, 2024.